Available online at www.sciencedirect.com
SCIENCE DIRECT®
Journal of Solid State Chemistry 173 (2003) 148–163
JOURNAL OF SOLID STATE CHEMISTRY
http://elsevier.com/locate/jssc

Structural aspects of $Pr_{1-x}Sr_xFeO_{3-w}$

Marit Stange,[a] Johan Lindén,[b] Arne Kjekshus,[a] Norman Binsted,[c] Mark T. Weller,[c] Bjørn C. Hauback,[d] and Helmer Fjellvåg[a,*]

[a] *Department of Chemistry, University of Oslo, P.O. Box 1033, Blindern, N-0315 Oslo, Norway*
[b] *Åbo Akademi, Physics Department, FIN-20500 Turku, Finland*
[c] *Department of Chemistry, University of Southampton, Southampton SO17 1BJ, UK*
[d] *Institute for Energy Technology, N-2007 Kjeller, Norway*

Received 14 March 2002; received in revised form 22 September 2002; accepted 23 October 2002

Abstract

Structural aspects of the distorted perovskite ABO_3 phase $Pr_{1-x}Sr_xFeO_{3-w}, x = 0.00–0.80, w = 0.000–0.332$, were studied by powder X-ray diffraction, powder neutron diffraction, ^{57}Fe Mössbauer spectroscopy, and Fe K-, Sr K-, and Pr L_{III}-edge EXAFS techniques. The diffraction data revealed no indications for ordering of Pr and Sr at the A site, nor for oxygen vacancy ordering at O sites for heavily reduced samples. Mössbauer spectroscopy showed octahedral, square pyramidal, and tetrahedral Fe coordinations with relative amounts closely following the predictions for a binomial distribution of oxygen vacancies. In addition to Fe^{3+} and Fe^{4+}, also Fe^{5+} appears at 77 K for (G-type) antiferromagnetic samples with high average Fe valence. This suggests dynamic 2 $Fe^{4+} \leftrightarrow Fe^{3+} + Fe^{5+}$ fluctuations. At 296 K, a mixed valence $Fe^{(3+n)+}$ component significantly improved the fit of Mössbauer spectra for the most oxidized paramagnetic samples. The qualitative EXAFS study shows that the local environments for Fe, Pr, and Sr strongly depend on x and w. The local Pr- and Sr-site geometries differ significantly from the cubic average structure for $Pr_{0.50}Sr_{0.50}FeO_{2.746}$.

1. Introduction

The corner sharing of octahedral building blocks turns perovskite-like arrangements into very flexible structures. With rather modest structural adjustments, a variety of elements can combine to give such ABX_3 atomic arrangements. Furthermore, one may introduce (heterovalent) substituents on the cationic sublattices, vacancies into the X sublattice (e.g., for $X = O$) in random or ordered ways, perovskite-like building blocks may be combined with blocks of NaCl or CaF_2 type, etc. Perovskite-like oxides possess a manifold of fascinating chemical and physical properties, e.g., colossal magnetoresistance, high-temperature superconductivity, mixed ionic–electronic conductivity, and charge, spin, and orbital ordering.

For the heterovalently substituted ferrites, $RE_{1-x}AE_xFeO_{3-w}$ (A site: RE = rare-earth element, AE = alkaline-earth element) the formal iron valence can be tuned by monitoring the degree of substitution and the oxygen-vacancy concentration. For the present solid solution, the formal iron valence varies from three in semiconducting, antiferromagnetic (AF) $PrFeO_3$ to four in metallic, AF $SrFeO_3$. Formal notations like Fe^{3+} and Fe^{4+} are used throughout the remainder of this paper.

Certain ferrites undergo charge mixing and charge separation (disproportionation). This involves formal iron oxidation states between Fe^{3+} and Fe^{5+} and was first noted for $CaFeO_3$ [1] where Fe^{4+} disproportionates into Fe^{3+} and Fe^{5+} below 115 K (see also Ref. [2]). $RE_{1-x}Sr_xFeO_{3-w}$; RE = La, Pr, Nd [3–13] exhibits corresponding charge phenomena, but shows in addition also an average mixed-valence state $Fe^{(3+n)+}$.

Phase relations, crystal and magnetic structures for $Pr_{1-x}Sr_xFeO_{3-w}$ have recently been described [14]. Extensive reports exist on the magnetic properties of $Pr_{1/3}Sr_{2/3}FeO_{3-w}$, $w < 0.1$ (space group $R\bar{3}c$) [7,11,15,16]. The many Mössbauer studies on $Pr_{1/3}Sr_{2/3}FeO_{3-w}$ indicate that Fe^{4+} exists above a certain temperature, below which it disproportionates into Fe^{3+} and Fe^{5+}. However, there is some disagreement concerning the temperature(s) involved (definitely

*Corresponding author. Fax: +47-22-855565.
E-mail address: helmerf@kjemi.uio.no (H. Fjellvåg).

0022-4596/03/$ - see front matter © 2002 Elsevier Science (USA). All rights reserved.
doi:10.1016/S0022-4596(02)00116-0

below room temperature), as to whether the disproportionation process is continuous (Fe^{4+} is definitely absent at 4.2 K), and whether or not non-integral charges are more appropriate for the iron ions (viz., $Fe^{(3+n)+}$, $Fe^{(4-m)+}$ etc.). In many reports on rare-earth ferrites $Fe^{(3+n)+}$ has been proposed as an independent average valence.

Upon topochemical reduction, the oxygen vacancies give rise to local configurations of FeO_5 and FeO_4. A random distribution of vacancies leads to iron configurations (CN = 6, 5, 4....) which follow the prescription of the binomial formula for $(RE_{2/3}Sr_{1/3})_3Fe_3O_8$, RE = Ce, Pr, Nd, Sm, Eu, Gd, Dy, and Y [7]. On the other hand, $La_{1/3}Sr_{2/3}FeO_{2.67}[(La_{1/3}Sr_{2/3})_3Fe_3O_8]$ exhibits vacancy ordering with FeO_6 and FeO_4 layers [17]. For $SrFeO_{2.86}$ ($Sr_8Fe_8O_{23}$) and $SrFeO_{2.75}$ ($Sr_4Fe_4O_{11}$) ordering of FeO_6 and FeO_5 entities occurs [18]. In the more strongly reduced brownmillerite-type phase $SrFeO_{2.50}$ ($Sr_2Fe_2O_5$), entities of FeO_6 and FeO_4 exist [18].

The clear structure-to-property relationship for perovskite-related oxides has basis in B–O–B interactions between corner-shared octahedra and involves overlap between oxygen s and p orbitals and transition-metal e_g and t_{2g} orbitals. For disordered solid-solution phases exact density-functional-theory calculations are not feasible. The desirable experimental description of the crystal structure on both average and local level, becomes challenging for $Pr_{1-x}Sr_xFeO_{3-w}$ owing to (i) difference in local structure stemming from two A elements (Pr and Sr) with quite different size, and (ii) local ordering of oxygen vacancies, in particular at high heterovalent substitution levels and under reducing (synthesis) conditions.

The present aim is to provide a detailed understanding of the atomic arrangement of $Pr_{1-x}Sr_xFeO_{3-w}$ on the average as well as local level. This is approached by combining powder X-ray diffraction (PXD) data that are sensitive to global symmetry lowering and to the Pr/Sr distribution, powder neutron diffraction (PND) data as a sensitive probe for the oxygen distribution, and to methods that are sensitive to the local structure, in this case Mössbauer spectroscopy for Fe and EXAFS for the Pr, Sr, and Fe coordinations.

2. Experimental

2.1. Synthesis

All samples were made according to the citric acid complexation method. Pr_6O_{11} was first dissolved in diluted nitric acid. Thereafter, appropriate amounts of $Fe(NO_3)_2 \cdot H_2O$, $SrCO_3$, and excess citric acid monohydrate were successively added (for details see Ref. [14]). Prior to the synthesis, Pr_6O_{11} and $SrCO_3$ were treated at 430°C in air to remove adsorbed water. The metal content of the iron nitrate hydrate was determined gravimetrically by complete decomposition to Fe_2O_3 at 1000°C.

After annealing in air at 900°C for 3 days and one intermittant grinding, the samples exhibited broad Bragg reflections [corresponding to Type I samples of Brinks et al. [14]]. A high degree of crystallinity was achieved after annealing in a stream of nitrogen gas at 1160°C for 48 h. Oxidized samples were obtained subsequently by annealing in air at 900°C for 24 h [oxidized Type II samples according to Brinks et al. [14]]. The number of oxygen vacancies (w) varied from $w = 0.00$ ($x = 0.00$) to $w = 0.158$ ($x = 1.00$) for air-synthesized samples and from $w = 0.109$ ($x = 0.20$) to $w = 0.332$ ($x = 0.67$) for reduced samples. All samples referred to in the result sections are phase pure.

Grossly oxygen non-stoichiometric, reduced samples were obtained by zirconothermic reduction of oxidized samples (viz. with analyzed oxygen content) in sealed ampoules at 800°C for 5 days. After slow cooling to 400°C over 7 days, the ampoules were finally quenched into ice/water mixtures. In order to prevent oxidation, all reduced samples were stored and handled in a glove box with argon-filled atmosphere.

2.2. Oxygen content analysis

The average oxidation state of iron was determined by cerimetric titration. The samples were dissolved in HCl (diluted with oxygen-free deionized water) under argon atmosphere. A specified amount of Mohrs salt was added to reduce all higher valent Fe species to Fe^{3+}. Thus remaining Fe^{2+} was (back)titrated with Ce^{4+} to establish the average iron valence and hence the oxygen content (i.e., w). Mohrs salt was also used to calibrate the Ce^{4+} titrant.

2.3. Powder X-ray diffraction

Powder X-ray-diffraction (PXD) data were collected with Siemens D5000 diffractometers in flat-plate transmission or reflection geometry using monochromatic Cu$K\alpha_1$ radiation from a Ge monochromator. The samples were evenly spread on Scotch magic tape or on a non-reflecting Si-plate, respectively. Silicon was used as internal standard and for calibration. Data were obtained in steps of $\Delta 2\theta = 0.015552°$ as defined by the Brown position-sensitive detector. The instrumental resolution in terms of FWHM for Si(111) is 0.07–0.09° and 0.10–0.11° for the two geometries, respectively. Unit-cell dimensions were determined by least-squares calculations using the program UNITCELL [19].

Low-temperature, high-resolution synchrotron PXD data were collected for $Pr_{0.50}Sr_{0.50}FeO_{3-w}$ at the Swiss–Norwegian beam line at ESRF, Grenoble, in capillary

geometry using monochromatic photons with wavelength $\lambda = 0.4997$ Å.

2.4. Powder neutron diffraction

Room temperature powder neutron-diffraction (PND) data were collected with the PUS two-axis diffractometer at the JEEP-II reactor at Kjeller, Norway. Air-sensitive samples were placed in vanadium cans and sealed with an indium washer. Monochromatized neutrons of wavelength $\lambda = 1.5549$ Å were obtained from Ge(511). Data were collected for the range $2\theta = 10$–130° in steps of 0.05° by means of two detector banks, each containing a stack of seven position-sensitive ^{3}He detectors and covering a range of 20° in 2θ. Room temperature time-of-flight (TOF) data for $PrFeO_3$ were measured at the high-intensity, medium-resolution, powder diffractometer Polaris at ISIS, UK. The diffracted beam is detected by ^{3}He backscattering detectors covering the 2θ range 130–160° (d spacing: 0.2–3.2 Å). Rietveld analyses were carried out for PXD and PND data using the GSAS software [20]. Adopted scattering lengths for Pr, Sr, Fe, and O were 4.45, 7.02, 9.54, and 5.81 fm, respectively, taken from the library of the program.

2.5. Magnetic properties

Magnetic susceptibilities of zero-field-cooled samples were measured in the temperature range 4–320 K, using a SQUID magnetometer (MPMS, Quantum Design).

2.6. Mössbauer spectroscopy

Mössbauer spectra were recorded at 77 and 296 K in transmission geometry using a maximum Doppler velocity of 15 and 1.5 mm/s for AF and paramagnetic (P) samples, respectively. An Amersham ^{57}Co:Rh (20 mCi, November 1998) source was used. The spectra were fitted with the full Hamiltonian of combined electric and magnetic interactions. The following hyperfine parameters were included in the fit: The internal magnetic field experienced by the Fe nucleus (B), the chemical isomer shift relative to α-Fe (δ), the quadrupole-coupling constant (eQV_{zz}), the resonance-line width (Γ), and the relative intensity of the components (I). The following conditions and constraints were applied: (i) For each component a certain variation in the parameter B was allowed in order to account for spread in the internal fields due to, e.g., local distortions of the coordination polyhedra. A Gaussian distribution was assumed and its width (ΔB) was introduced as a fitting parameter. Possible lattice strains could lead to a corresponding distribution for eQV_{zz}. However, the simultaneous fitting of such distributions for two different hyperfine parameters is hardly feasible. For the fitting of the P spectra, where B and ΔB were set equal to zero, a Gaussian distribution was introduced on eQV_{zz}, the width of which being given by the fitting parameter ΔV_{zz}. Only one common ΔV_{zz} was used for all components. (ii) Owing to the pseudo-cubic character of the structures, the asymmetry parameter η and the angle θ between the direction of the magnetic and electric quantization axes were kept fixed. A consequence of this averaging for θ is that the eQV_{zz} values for AF spectra are generally smaller than those for P spectra. (iii) All components were constrained to have equal Γ. Γ increases near T_N, which also effects ΔB. (iv) A small asymmetric quadrupole component (originating from traces of Fe in the Be detector window and in the Al foil) was kept fixed during the fitting. These impurity signals cover less than 2% of the total spectral intensity.

2.7. EXAFS data

Room temperature, extended X-ray-absorption fine-structure (EXAFS) data were collected in transmission mode at the Daresbury Laboratory Synchrotron Radiation Source on the beam lines 8.1 [Pr L_{III}- and Fe K-edges; Si(111) double-crystal monochromator] and 9.2 [Sr K-edge; Si(220) monochromator]. The samples were ground in an agate mortar and sieved through a 15 μm mesh. The fine powder was thereafter mixed with polyvinyl alcohol. Pellets were pressed and put into a 1.2 cm^2 hole in a 1 mm thick aluminum disk. All reduced samples were handled as if being air sensitive and the flat pellets were covered with kapton tape. The tape edges were sealed with super-epoxy glue. Between two and four scans were averaged for each specimen. Background subtraction was performed by means of the program PAXAS [21]. Analyses of EXAFS data were carried out with the Southampton software [22].

3. Results and discussion

3.1. Average structure of $Pr_{1-x}Sr_xFeO_{3-w}$ (oxidized; $w \approx 0.00$)

The crystalline perfection of $Pr_{1-x}Sr_xFeO_{3-w}$ (as seen by FWHM for PXD and PND data) depends strongly on the entire annealing history of the samples. Heat treatment of the citrate precursor at 900°C gave samples with FWHM about twice the instrumental resolution. This most probably reflects a non-random distribution of Pr and Sr over the A site. On turning to higher annealing temperature (1160°C) A-site cation diffusion is enhanced. The peak widths then correspond roughly to the instrumental resolution [typically FWHM $\approx 0.09^\circ$ at $2\theta \approx 33^\circ$ for $x = 0.33$ with small orthorhombic splitting]. The poorer quality of samples annealed at 900°C implied that their symmetry could not be

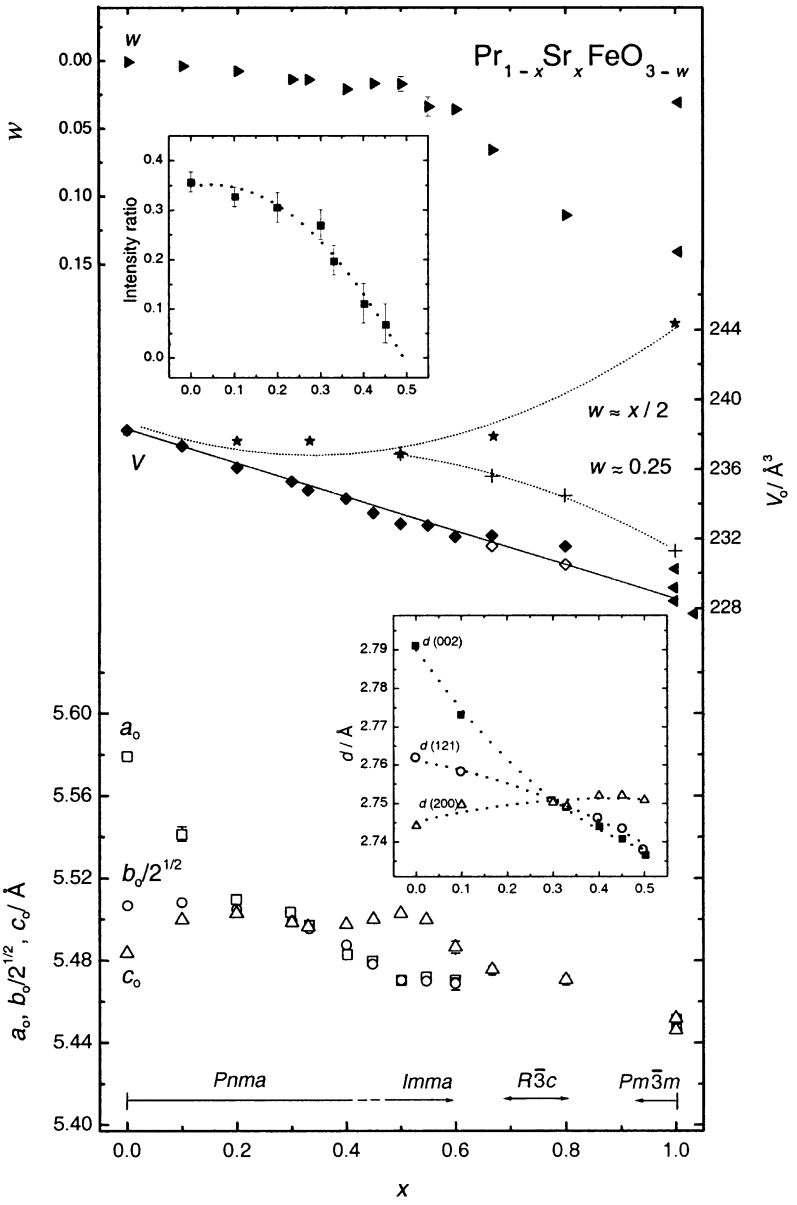

Fig. 1. Unit-cell dimensions vs. x for $Pr_{1-x}Sr_xFeO_{3-w}$. Cerimetrically determined oxygen content (w) is given for oxidized samples. ○ refers to unit-cell volume corrected (see text) for the effect of differences in w. Values (marked ◀) for $SrFeO_3$ and $SrFeO_{2.86}$ are taken from Refs. [18,29]. Space-group symbols are included at the bottom of the illustration. Left inset: Intensity ratio $(I[(113),(311)]/I[(101),(020)])$ for $0.00 \leqslant x \leqslant 0.50$. Right inset: $d(200)$, $d(121)$, and $d(002)$ for $0.00 \leqslant x \leqslant 0.50$. Unless specifically marked (★, +) data refers to oxidized samples.

unequivocally settled; for $x \leqslant 0.40$ orthorhombic and for $x = 0.50$–0.80 probably rhombohedral.

The unit-cell dimensions for high-quality, oxidized samples annealed at 1160°C are shown in Fig. 1. $PrFeO_3$ and the Pr-rich region of $Pr_{1-x}Sr_xFeO_{3-w}$ ($w \approx 0.00$) crystallize with the $GdFeO_3$-type structure in space group *Pnma* [23]. The present refinements of PXD and PND data for $x < 0.50$ (see also Ref. [14]) exclude long-range order of Pr and Sr. Numerical data for the structural parameters are given in Table 1.

Inspection of certain characteristic intensities in the diffraction diagrams indicates a continuous conversion (completed for $x \approx 0.50$ at 296 K) of space-group symmetry from *Pnma* to *Imma* (*I*2/*m* and *I*2/*a* also considered) with increasing x. The left inset to Fig. 1 shows the intensity ratio of the in-pairs overlapping PXD reflections $[I(113) + I(311)]$ (allowed in *Pnma*, extinct in *Imma*) to $[I(101) + I(020)]$ (allowed in *Pnma* and *Imma*). The axial ratios are different in the two regimes: $a > b/\sqrt{2} > c$ for $x < 0.33$; $c > a \approx b/\sqrt{2}$ for $0.33 < x < \sim 0.6$. The possibility of a trivial two-phase situation (two pseudo-cubic phases, one orthorhombic and one pseudo-cubic phase or two orthorhombic phases) in the latter range was ruled out by: (i) Variation

Table 1
Atom coordinates and interatomic distances in $PrFeO_3$, $Pr_{0.80}Sr_{0.20}FeO_{2.993}$ (space group *Pnma*), and $Pr_{0.50}Sr_{0.50}FeO_{2.983}$ (space group *Imma*) from Rietveld refinement of PND data[a]

Parameter	$PrFeO_3$	$Pr_{0.80}Sr_{0.20}FeO_{2.993}$	$Pr_{0.50}Sr_{0.50}FeO_{2.983}$
a_O (Å)	5.5737(2)	5.5195(2)	5.4695(2)
b_O (Å)	7.7869(2)	7.7838(3)	7.7354(3)
c_O (Å)	5.4831(2)	5.5014(2)	5.5036(2)
$x_{Pr(Sr)}$	0.0440(5)	0.0289(5)	
$z_{Pr(Sr)}$	0.9889(7)	0.995(1)	0.0012(7)
x_{O1}	0.4783(9)	0.4877(5)	
z_{O1}	0.0821(8)	0.0750(7)	−0.0517(7)
x_{O2}	0.2923(5)	0.2834(3)	
y_{O2}	0.0431(4)	0.0385(3)	−0.0279(3)
z_{O2}	0.7072(5)	0.7173(3)	
Fe–O (Å)	$2\times2.002(1), 2\times2.008(2)$	$2\times1.985(2), 2\times1.990(1)$	$4\times1.952(1), 2\times1.955(1)$
	$2\times2.014(2)$	$2\times1.991(2)$	
Fe–Pr/Sr (Å)	$2\times3.202(1), 2\times3.322(3)$	$2\times3.248(2), 2\times3.349(4)$	$4\times3.349(3), 2\times3.358(3)$
	$2\times3.421(4), 2\times3.604(3)$	$2\times3.397(4), 2\times3.509(2)$	$2\times3.369(3)$
Fe–Fe (Å)	$2\times3.894(1), 4\times3.909(1)$	$2\times3.892(2), 4\times3.896(1)$	$2\times3.868(1), 4\times3.880(1)$
Pr/Sr–O (Å)	$2.381(3), 2\times2.392(4), 2.473(3)$	$2.379(7), 2\times2.430(4), 2.570(3)$	$2.474(5), 4\times2.588(2)$
	$2\times2.627(3), 2\times2.736(3)$	$2\times2.648(4), 2\times2.760(3)$	$2\times2.750(1), 4\times2.899(2)$
	$3.153(3), 3.194(3), 2\times3.391(3)$	$3.020(4), 3.142(7), 2\times3.244(3)$	3.030(5)
Pr/Sr–Pr/Sr (Å)	$2\times3.825(5), 2\times3.926(5)$	$2\times3.855(8), 2\times3.938(8)$	$2\times3.868(1), 2\times3.870(1)$
	$2\times3.995(6)$	$2\times3.905(5)$	$2\times3.889(5)$
Fe–O1–Fe (deg)	153.07(12)	155.75(13)	163.80(9)
Fe–O2–Fe (deg)	152.82(7)	157.07(12)	166.28(11)
$B_{Pr/Sr}$ (Å^2)	0.28(7)	0.55(4)	0.39(3)
B_{Fe} (Å^2)	0.23 (3)	0.18(2)	0.15(2)
B_O (Å^2)	0.45(3)	0.72(3)	1.08(2)
μ_{Fe} (μ_B)	4.07(5)	2.86(2)	—
R_P (%)	3.91	4.25	6.08

[a] Calculated standard deviations are given in parentheses.

in $d(200)$, $d(121)$, and $d(002)$ (positions determined by profile analysis; right inset to Fig. 1). (ii) PXD and PND Rietveld refinements of diffraction data for $x = 0.50$. (iii) Only one signature of a Néel temperature in the magnetic susceptibility data (see Section 3.3).

Results from Rietveld refinements for $x = 0.50$ in the *Imma* model are given in Table 1. The calculated bond valences are Pr: 2.62; Sr: 2.48, and Fe: 3.57. The latter compares well with the mean oxidation state of Fe (3.46), but those for Pr and Sr deviate significantly. Site-bond valences generally agree well with expected values [e.g., 3.05 for Pr in $PrFeO_3$ [23]] but complexities arise in solid-solution phases owing to local variations in oxygen distances.

For $x \geqslant 0.67$ the rhombohedral $R\bar{3}c$ tilt system [24,25] appears to provide the best fit to the PXD data. The likely alternative space groups $Pm\bar{3}m$ and $I4/mcm$ did not reproduce the observed splittings and intensities. Oxidized samples with compositions close to $SrFeO_3$ take the simple perovskite-aristotype arrangement ($Pm\bar{3}m$), whereas for reduced samples oxygen vacancy-ordered superstructures may occur, see Ref. [14]. A two-phase region is expected between the region with continuous conversion from *Pnma* to *Imma* symmetry and the $R\bar{3}c$ region, but could not be confirmed experimentally. Two-phase regions are reported for $La_{1-x}Sr_xFeO_{3-w}$ [8] synthesized in air (between *Pnma* and $R\bar{3}c$ around $x = 0.30$ and between $R\bar{3}c$ and a tetragonal phase for $0.60 \leqslant x \leqslant 0.90$), however, not for other $RE_{1-x}Sr_xFeO_{3-w}$ phases. A conversion from *Pnma* to *Imma* symmetry is reported [26] for the $RE_{0.50}Sr_{0.50}MnO_3$ series as the size of *RE* is increased from Gd to Pr. For even larger-sized *RE*s the $I4/mcm$ symmetry is observed.

Tilting of octahedra [25] is by far the most common deformation mechanism for perovskites. By means of the POTATO program [27], the observed lattice parameter vs. x relationships (Fig. 1) were aimed simulated by changes in tilt angles. The starting point was the $a^-b^+a^-$ tilt system (*Pnma*). The two tilt angles were gradually varied, first making the b^+ tilt angle the largest, then a^- and b^+ equal before decreasing b^+ to zero ($a^-b^0a^-$ according to *Imma*). One could thereby simulate a conversion from three differently sized "axes", via an interregnum with numerically equal "axes" to a range with just two approximately equal "axes".

The mechanism for a similar tilt sequence in $RE_{0.5}Sr_{0.5}MnO_3$ has been attributed to the size of *RE* by Woodward et al. [26]. However, the structural explanation must be more complex for $Pr_{1-x}Sr_xFeO_{3-w}$ since, although the radius [CN = 9 [28]] of Sr^{2+} is 10%

larger than that of Pr^{3+}, the unit-cell volume decreases with x. Further, the present XRD data show no indication of short-range layered order as has been suggested by Woodward et al. [26] for $RE_{0.5}Sr_{0.5}MnO_3$. Woodward et al. point out a possible correlation between symmetry and cooperative magnetism, but no such clear correlations appear for $Pr_{1-x}Sr_xFeO_{3-w}$ (see Section 3.3). However, a factor that presently must be taken into account is the (x, w)-dependent proportion of higher-valent iron that affects the average size of the FeO_6 octahedra, and thereby also tilt angles and unit-cell volume. Simultaneously, there may occur a change in the bonding characteristics (and electronic structure) with increasing x.

The unit-cell volume ($V_0; Z = 4$) contraction is linear for $0.00 \leqslant x \leqslant 0.60$ ($w \approx 0.00$), Fig. 1. The extrapolated $V_0(x = 1.00)$ corresponds well to high-oxygen-pressure-synthesized $SrFeO_3$ [18,29]. The enlarged volumes for the $x = 0.67$ and 0.80 samples are attributed to oxygen non-stoichiometry and comply reasonably well with that for air-annealed $SrFeO_{2.86}$ [18]. On adjusting these two V_0 values with a factor corresponding to the chemical expansion for $SrFeO_{3-w}$ ($0.00 \leqslant w \leqslant 0.25$), all $V_0(x)$ data obey the linear relationship (see Fig. 1).

3.2. Average structure of reduced $Pr_{1-x}Sr_xFeO_{3-w}$

Reduced samples of $Pr_{1-x}Sr_xFeO_{3-w}$ with oxygen contents corresponding to solely Fe^{3+} ($w = x/2$) were made at 800°C by topotactic reduction, primarily with focus on sample quality for EXAFS and Mössbauer spectroscopy studies. Some relevant data are shown in Fig. 1 for reduced samples with $w \approx 0.25$ and $w \approx x/2$. None of these showed superstructure reflections indicative of vacancy ordering. For samples with $x \geqslant 0.33$ there is no peak broadening that could indicate reduction of the cubic symmetry [FWHM(011) typically 0.10°], even when investigated by high-resolution synchrotron PXD at 10 K ($Pr_{0.50}Sr_{0.50}FeO_{2.752}$). Upon reduction, the orthorhombic *Pnma* regime shrinks considerably, and there is no sign of any region with *Imma* or *I*4/*mcm* symmetry. An approximately linear relationship is established between unit-cell volume and w for $x = 0.50$ ($w = 0.017$, 0.144, and 0.248).

The oxidized samples with small FeO_6 octahedra exhibit considerable tilting and orthorhombic deformation for $x \leqslant \sim 0.6$. One would expect enhancement of these features when the larger Fe^{3+} in the reduced samples replaces Fe^{4+}. The deviating behavior of the reduced samples is likely to be due to the vast number of oxygen vacancies that locally will give rise to FeO_5 square pyramids and FeO_4 tetrahedra. It is likely that a framework composed of randomly distributed, variously deformed and oriented octahedra, square pyramids, and tetrahedra will average to a cubic arrangement. However, this occurs at the expense of efficient packing, hence, a volume increase is observed. In addition, the linkage between defect polyhedra, Fe–O bond-length adjustments, and clustering of, say, Sr^{2+} around oxygen vacancies may complicate the picture even more.

In the Rietveld PND refinements, the oxygen vacancies were for simplicity accounted for as $(3 - w)/3$ occupancy of the oxygen site in $Pm\bar{3}m$. The unit-cell dimensions are; $Pr_{0.50}Sr_{0.50}FeO_{2.752}$; $a_c = 3.9001(1)$ Å, $Pr_{0.33}Sr_{0.67}FeO_{2.668}$; $a_c = 3.9062(2)$ Å, $Pr_{0.33}Sr_{0.67}FeO_{2.751}$; $a_c = 3.8904(3)$ Å and $Pr_{0.20}Sr_{0.80}FeO_{2.746}$; $a_c = 3.8846(2)$ Å, with moderate R factors (R_P) around 8.2% (see also Section 3.5).

3.3. Magnetic properties

The magnetic susceptibility curves for oxidized Fe^{3+} and Fe^{4+} bearing samples, show a clear anomaly around the AF ordering temperature, T_N (see also Ref. [14]). For all reduced samples containing just Fe^{3+}, T_N is high and approximately constant (ca. 700 K, see Fig. 2). Introduction of Fe^{4+} by oxidation lowers T_N below 298 K at $x > 0.40$ for air-synthesized samples. Indeed, T_N strongly depends on the average iron valence (v_{Fe}), and over the interval $0.40 \leqslant x \leqslant 0.60$ it is reduced from 308 ($v_{Fe} = 3.35$) to 185 K ($v_{Fe} = 3.53$). In the earlier study [14] T_N for a sample with $x = 0.50$, $w = 0.06$($v_{Fe} = 3.38$) was incorrectly reported as 440 K.

The compositional independence of T_N for samples that contain solely Fe^{3+} (Fig. 2) may be rationalized according to the molecular field expression [34]: $T_N = [2S(S+1)/3k] \sum_i z_i J_i$. Since the oxidation state and the magnetic moment (S) of Fe is maintained constant, the compositional invariance of T_N implies that changes in the exchange interaction parameters J_i compensate for the effective decrease in the number of nearest magnetic neighbors z_i consequent on the decreased oxygen content within the series.

The lowering of T_N upon introduction of Fe^{4+} complies with findings for $La_{1-x}Sr_xFeO_{3-w}$ [35]. A simple explanation would be the lower magnetic moment for Fe^{4+}. However, since T_N for samples oxidized under oxygen pressure is somewhat above those oxidized in air (see Fig. 2) this cannot be the complete story. In fact, it is obvious that J_i varies with the details of the average and/or local structure [say Fe–O–Fe bond angle, charges of the Fe atoms (see Section 3.4), etc.].

The inverse magnetic susceptibility curves for air-oxidized samples with $x \leqslant 0.40$ usually show a slight change in slope around 100 K. The origin of this feature is not identified. Finally, it should be noted that the Curie–Weiss paramagnetic moments derived from the limited P regions of the susceptibility curves between T_N and 320 K, are generally higher than expected according to the analytical amounts of Pr^{3+}, Fe^{3+},

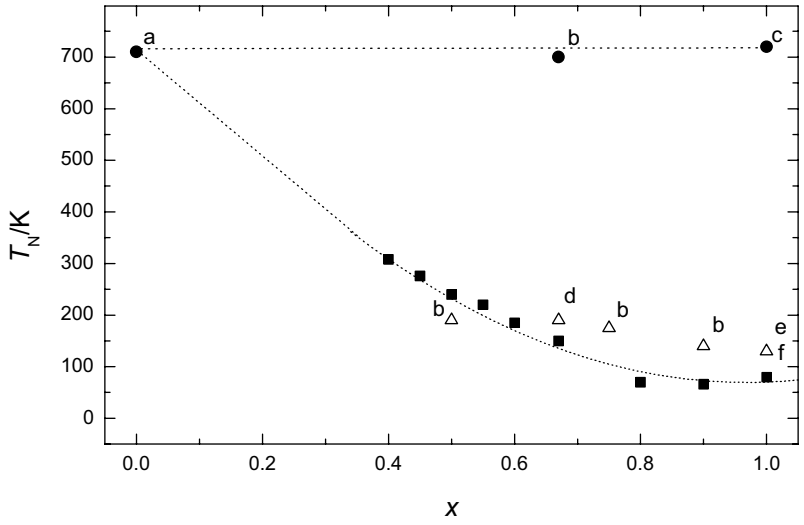

Fig. 2. Dependence of T_N on x and w in $Pr_{1-x}Sr_xFeO_{3-w}$. Points marked •: samples containing Fe^{3+} only ($w = x/2$), ■: samples synthesized in air (see Fig. 1), and △: samples oxidized under O_2 pressure. Lines are guides for the eye. References for quoted results: a: [30], b: [14], c: [31], d: [11], e: [32], and f: [33].

and Fe^{4+}. The refined magnetic moments at 296 K from PND data for $Pr_{0.50}Sr_{0.50}FeO_{2.752}$, $Pr_{0.33}Sr_{0.67}FeO_{2.668}$, and $Pr_{0.33}Sr_{0.67}FeO_{2.751}$ (all G-type antiferromagnets) are 4.03(3), 4.01(4), and 3.02(4) μ_B, respectively.

3.4. Mössbauer studies

The iron species in the investigated samples may have several formal valence states: Fe^{3+}, Fe^{4+}, Fe^{5+} or mixed (average, non-integral) valence $Fe^{(3+n)+}$, and local coordinations: octahedral CN = 6, square pyramidal CN = 5, and to lesser extent CN = 4 (deformed tetrahedral). The species are specified with coordination number (CN), valence (N+), magnetic state (M), and spin quantum number (S: assuming spin-only), in shorthand ${}^{CN}_{M}Fe^{N+}_{S}$. In fitting the AF spectra a maximum of six components were used, tentatively assigned as ${}^{CN6}_{AF}Fe^{5+}_{S3/2}$, ${}^{CN6}_{AF}Fe^{4+}_{S2}$, ${}^{CN6}_{AF}Fe^{3+}_{S5/2}$, ${}^{CN5}_{AF}Fe^{3+}_{S5/2}$, ${}^{CN4}_{AF}Fe^{3+}_{S5/2}$, and/or ${}^{CN5}_{AF}Fe^{2+}_{S2}$ on the basis mainly of isomer shift and internal magnetic field parameters. The ${}^{CN6}_{AF}Fe^{5+}_{S3/2}$ component occurs only in spectra recorded below ca. 200 K, in accordance with previous reports [11–13,15]. The P spectra consist of overlapping doublets. Among the six components ${}^{CN6}_{P}Fe^{4+}$, ${}^{CN6}_{P}Fe^{(3+n)+}$, ${}^{CN5}_{P}Fe^{(3+n)+}$, ${}^{CN6}_{P}Fe^{3+}$, ${}^{CN5}_{P}Fe^{3+}$, and ${}^{CN4}_{P}Fe^{3+}$ no more than four were used to fit a single P spectrum. The relative intensities of the components depend on x, w, and temperature.

3.4.1. AF spectra recorded at 296 K

Examples of fitted AF spectra are shown in Fig. 3. Spectral assignments are given in Table 2. The well-defined ${}^{CN6}_{AF}Fe^{3+}_{S5/2}$ in $PrFeO_3$ (the additional 2% ${}^{CN5}_{AF}Fe^{2+}_{S5/2}$ was not detected by PXD) is followed by the new components: ${}^{CN6}_{AF}Fe^{4+}_{S2}$ upon increasing x plus ${}^{CN5}_{AF}Fe^{3+}_{S5/2}$ upon increasing x and w. On reduction for a given x ${}^{CN6}_{AF}Fe^{4+}_{S2}$ loses intensity, whereas ${}^{CN5}_{AF}Fe^{3+}_{S5/2}$ gains intensity. On further reduction ${}^{CN4}_{AF}Fe^{3+}_{S5/2}$ appears. The most reduced sample $Pr_{0.33}Sr_{0.67}FeO_{2.668}$ contains 13% of this component (Table 2 and Fig. 3). For the most reduced samples, traces (2–6%) of a possible divalent impurity were seen. This component is not included in the following discussion. Several spectra exhibit large line broadening (typical line width 0.45–0.60 mm/s) reflecting that T_N is close to room temperature. The P state of $x = 0.45$ at 296 K is in accordance with Fig. 2. Broadening also arises from dynamic effects related to the disproportionation of Fe^{4+} (plus), and the shortcomings of just using static components in the fitting was dealt with by introducing one (or two) additional six-coordinated Fe^{4+} "satellite" component(s).

3.4.2. AF spectra recorded at 77 K

The 77 K AF spectra (Fig. 4 and Table 2; typical line width 0.35–0.45 mm/s) exhibit one additional component not present at 296 K, ${}^{CN6}_{AF}Fe^{5+}_{S3/2}$, which results from a temperature-dependent disproportionation of Fe^{4+} to Fe^{5+} and Fe^{3+} in samples with high average iron valence. At 77 K the satellites of ${}^{CN6}_{AF}Fe^{4+}_{S2}$ are no longer detectable in most spectra. On the other hand, the asymmetry of the resonance line for, e.g., $x = 0.50, w = 0.017$ can only be explained by one additional ${}^{CN6}_{AF}Fe^{3+}_{S5/2}$ component ("satellite"). This may also reflect the dynamic charge-disproportionation process, which naturally affects the amount of ${}^{CN6}_{AF}Fe^{3+}_{S5/2}$. The hyperfine parameters of this "satellite" are in all aspects closely related to those of the main component. The "satellite" may alternatively be interpreted in terms of asymmetry in the internal field distribution.

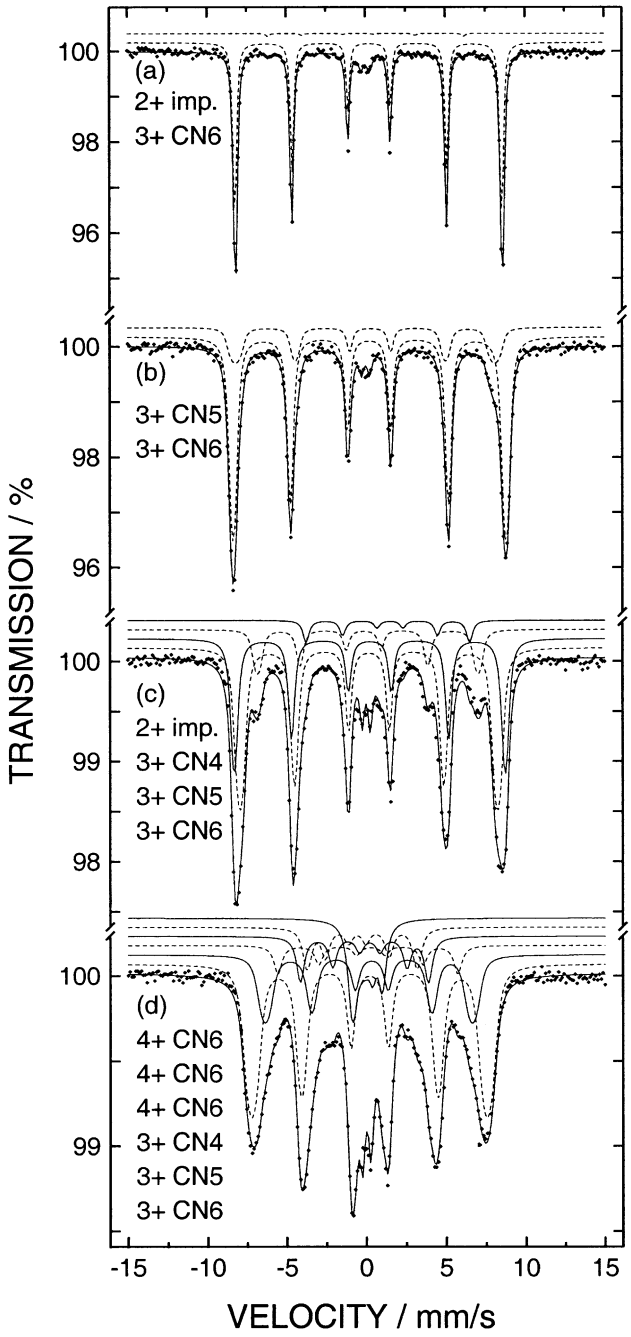

Fig. 3. Selected fitted AF ^{57}Fe Mössbauer spectra (296 K) for (a) $x = 0.00$, $w = 0.00$, (b) $x = 0.20$, $w = 0.111$, (c) $x = 0.67$, $w = 0.332$, and (d) $x = 0.50$, $w = 0.144$. For each spectrum the assigned spectral components are shown above the fitted data in the order presented on the left-hand side.

3.4.3. P spectra

In the P spectra of the fully oxidized samples two components assigned to six-coordinated Fe species dominate (Fig. 5b and Table 3; typical line width 0.25–0.35 mm/s). These strongly overlapping components appear as a broad asymmetric resonance line centered close to zero velocity. Their relative intensities do not match the portions of Fe^{4+} and Fe^{3+} and are tentatively assigned $^{CN6}_{P}Fe^{4+}$ and $^{CN6}_{P}Fe^{(3+n)+}$, as suggested in earlier studies [5–7]. At least one of these components reflects a fluctuating mixed-valence state. Upon increasing temperature it is expected to approach the average Fe valence obtained from titration with a consequent disappearance of the Fe^{4+} component. Upon reduction the ordinary $^{CN5}_{P}Fe^{3+}$ component appears. On further reduction even $^{CN4}_{P}Fe^{3+}$ is found. In the most reduced sample $x = 0.80, w = 0.254$ this $^{CN4}_{P}Fe^{3+}$ component covers 10% of spectral intensity (Fig. 5a). For this sample only integral valence states were observed, i.e., an increase in w may stabilize integral valence states.

The P spectra for oxygen deficient $SrFeO_{3-w}$ (i.e., $x = 1$) depend strongly on the vacancy concentration and crystal structure. The spectrum for $w = 0.158$ is dominated by $Fe^{(3+n)+}$ and Fe^{4+} while that for $w = 0.260$ by Fe^{3+} and Fe^{4+} species. Fournés et al. [36] showed that an overall average Fe-valence state occurs above some 600–700 K. In accordance with earlier findings [37,38] Fe^{4+} prefers CN = 5 and Fe^{3+} CN = 6, which implies that the vacancies are not binomially distributed. For $SrFeO_{3-w}$ the CN = 4 configurations observed for oxygen-disordered $Pr_{1-x}Sr_xFeO_{2.75}$ do first appear at lower oxygen stoichiometry, i.e., for ordered $Sr_2Fe_2O_5$ [23].

3.4.4. Assignments

3.4.4.1. Internal magnetic field (AF samples). At 77 K the internal field values are normally nearly saturated. High-spin Fe^{3+} species $^{CN6}_{AF}Fe^{3+}_{S5/2}$ or $^{CN5}_{AF}Fe^{3+}_{S5/2}$ have internal field values of around 37–56 T at 77 K. In comparison, $LaBa_2Fe_3O_{8+w}$ at 85 K [37] exhibits field values of 46–55 and 37–54 T for $^{CN6}_{AF}Fe^{3+}_{S5/2}$ and $^{CN5}_{AF}Fe^{3+}_{S5/2}$, respectively. Owing to the lower CN the saturation fields are lower for $^{CN5}_{AF}Fe^{3+}_{S5/2}$. This complies well with findings (37–43 T, 290 K) for $RESr_2Fe_3O_8$ [7]. Small amounts of $^{CN4}_{AF}Fe^{3+}_{S5/2}$ were identified in some reduced samples.

At 77 K oxidized samples with higher valent Fe species exhibit one or two components with internal fields of 21–31 T. Although limited data are available for Fe^{4+} and Fe^{5+}, the findings comply with 27–28 T for $^{CN6}_{AF}Fe^{4+}_{S2}$ in $SmBaFe_2O_{5.6}$ [38], 26 T for $^{CN6}_{AF}Fe^{5+}_{S3/2}$ in $LaSr_2Fe_3O_{8.94}$ [6], and 28 T for $^{CN6}_{AF}Fe^{5+}_{S3/2}$ in $Sr_3Fe_2O_7$ [39]. The assignment of these exotic Fe species required consideration of all hyperfine parameters. The spectra for $x = 0.50, w = 0.144$, $T = 296$ K; $x = 0.67$, $w = 0.249$, $T = 296$ K; and $x = 0.80$, $w = 0.254$, $T = 77$ K all show broad line widths that were modelled by three Fe^{4+} components. Two of these with B ca. 21 and 24 T, were assigned to $^{CN6}_{AF}Fe^{4+}_{S2}$ with an asymmetric distribution of the hyperfine parameter. The third component has an unusually low internal field of ca. 6 T. This additional complexity may arise from discrepancies in the fitting of the more intense components or fast

Table 2
Mössbauer parameters (B, δ, eQV_{zz}, I) for antiferromagnetic (AF) state $Pr_{1-x}Sr_xFeO_{3-w}$ at 77 and 296 K (in italics)

x[a]	w	$^{CN6}_{AF}Fe^{3+}_{S5/2}$	$^{CN5}_{AF}Fe^{3+}_{S5/2}$	$^{CN4}_{AF}Fe^{3+}_{S5/2}$	$^{CN6}_{AF}Fe^{4+}_{S2}$	$^{CN6}_{AF}Fe^{5+}_{S3/2}$	$^{CN6}_{AF}Fe^{3+}_{S5/2}$	$^{CN5}_{AF}Fe^{3+}_{S5/2}$	$^{CN4}_{AF}Fe^{3+}_{S5/2}$	$^{CN6}_{AF}Fe^{4+}_{S2}$	$^{CN6}_{AF}Fe^{5+}_{S3/2}$
		$B(T)$					δ (mm/s)				
0.00[b]	*0*	*51.966(7)*					*0.3185(9)*				
0.20	0.007(1)	55.8/54.0	50.1(3)	—	31.1(2)	26.5(1)	0.430/0.394	0.40(2)	—	0.18(4)	−0.08(1)
0.20	*0.007(1)*	*48.9/42.6*	*37.0*	—	*27.8/19.1*		*0.322/0.278*	*0.222*		*0.053/−0.044*	
0.20	*0.109(6)*	*53.13(2)*	*50.5(2)*	—	—	—	*0.324(2)*	*0.22(1)*	—	—	—
0.50	0.017(5)	49.53(8)/49.83(9)	37.2(5)	—	29.0(2)	26.23(9)	0.34(1)/0.41(1)	0.43(8)	—	0.05(2)	−0.076(9)
0.50	0.144(1)	51.83(8)	50.6(2)	38.9(6)	30.6(3)	26.1(2)	0.403(4)	0.35(1)	0.26(7)	0.12(4)	−0.02(3)
0.50	*0.144(1)*	*45.8(2)*	*40.3(5)*	*35.0(3)*	*21.4(2)/24.9(3)/6.0(1)*[c]		*0.291(8)*	*0.33(1)*	*0.28(2)*	*−0.32(2)/0.15(2)/0.04(1)*[c]	
0.50[b]	0.248(2)	56.20(7)	53.2(2)	48.7(4)			0.408(5)	0.35(1)	0.24(5)		
0.50[b]	*0.248(2)*	*56.9(1)*	*53.9(2)*	*50* (fixed)			*0.347(8)*	*0.22(2)*	*0.50(4)*		
0.67	0.065(1)	44.3(1)/50.8(3)	39.1(3)	—	25.3(2)/6.4(1)[c]	21.3(6)	0.37(1)/0.41(4)	0.49(fixed)	—	−0.02(1)/0.14(2)[c]	−0.11(4)
0.67	0.249(2)	53.9(1)	51.0(3)	42.3(5)	31.2(4)	25.1(2)	0.41(1)	0.33(2)	0.62(6)	−0.02(5)	−0.00(3)
0.67	*0.249(2)*	*46.9(2)*	*41.8(4)*	*36.9(5)*	*21.7(3)/24.0(5)/5.7(2)*[c]		*0.278(8)*	*0.31(1)*	*0.38(4)*	*0.06(5)/−0.30(4)/0.06(4)*[c]	
0.67[b]	0.332(3)	53.8(2)	56.1(1)	47.3(2)			0.373(8)	0.43(1)	0.22(2)		
0.67[b]	*0.332(3)*	*50.13(7)*	*52.77(6)*	*42.73(8)*			*0.268(3)*	*0.326(3)*	*0.080(9)*		
0.80	0.254(2)	48.1(3)	43.1(5)	36.9(6)	27.2(3)/21.2(3)/7.4(3)[c]		0.39(3)	0.30(3)	0.51(fixed)	0.14(5)/−0.03(3)/0.35(4)[c]	
eQV_{zz} (mm/s)							I (%)				
0.00[b]	*0*	*−0.063(4)*	—	—	—		*98(1)*				
0.20	0.007(1)	−0.08/−0.09	−0.00(8)		−0.2(2)	−0.06(5)	30(3)/53(3)	6(1)	—	2(1)	9(1)
0.20	*0.007(1)*	*−0.16/0.04*	*0.27*		*0.32/0.88*		*41/25*	*12*	—	*13/9*	
0.20	*0.109(6)*	*−0.03(1)*	*−0.72(5)*	—	—	—	*79(1)*	*21(1)*			
0.50	0.017(5)	−0.6(1)/0.4(1)	−0.0(3)		−0.10(8)	0.10(4)	36(3)/33(2)	1(1)		11(1)	19(1)
0.50	0.144(1)	−0.07(2)	−0.04(5)	0.4(3)	−0.2(1)	0.2(1)	62(3)	21(2)	2(1)	5(1)	11(1)
0.50	*0.144(1)*	*−0.08(4)*	*−0.41(5)*	*−0.41(8)*	*0.59(8)/−0.71(9)/0.39(5)*[c]		*47(4)*	*20(3)*	*5(1)*	*8(1)/8(1)/12(1)*[c]	
0.50[b]	0.248(2)	0.06(2)	−0.19(4)	−0.4(2)			57(3)	33(3)	6(1)		
0.50[b]	*0.248(2)*	*0.05(2)*	*0.03(4)*	*0.2(fix)*			*49(3)*	*39(3)*	*6(1)*		
0.67	0.065(1)	−0.09(3)/−1.4(1)	−0.6(1)	—	−0.08(4)/0.55(7)[c]	0.3(1)	38(1)/5(1)	9(1)		31(2)/8(1)[c]	8(2)
0.67	0.249(2)	−0.01(3)	−0.1(5)	−0.1(2)	−0.6(2)	−0.0(1)	48(3)	35(3)	3(1)	4(1)	10(1)
0.67	*0.249(2)*	*0.01(3)*	*−0.26(5)*	*−0.66(2)*	*−1.1(2)/0.8(2)/0.3(1)*[c]		*45(3)*	*26(2)*	*5(1)*	*6(1)/8(1)/9(1)*[c]	
0.67[b]	0.332(3)	−0.06(3)	−0.06(4)	0.15(9)			49(4)	34(4)	14(1)		
0.67[b]	*0.332(3)*	*−0.08(1)*	*−0.07(1)*	*0.47(4)*			*50(1)*	*32(2)*	*13(1)*		
0.80	0.254(2)	0.0(1)	0.2(1)	−0.5(3)	0.6(2)/0.4(1)/0.5(2)[c]		36(2)	17(3)	7(1)	12(1)/16(2)/11(1)[c]	

[a] Some spectra could not be fitted: $x = 0.10$, $w = 0.003(3)$, $T = 296$ K, AF state, very asymmetric; $x = 0.33$, $w = 0.013(5)$, $T = 296$ K, AF state, large line widths; $x = 0.40$, $w = 0.020(4)$, $T = 296$ K, AF state wings superimposed on P-state main features; $x = 0.80, w = 0.113(5)$, $T = 77$ K, T_N slightly above 77 K, one broad peak of AF-state features.

[b] Additional $^{CN5}_{AF}Fe^{2+}_{S2}$ species with I between 2% and 6%.

[c] Possibly $^{CN6}_{AF}Fe^{4+}_{S1}$.

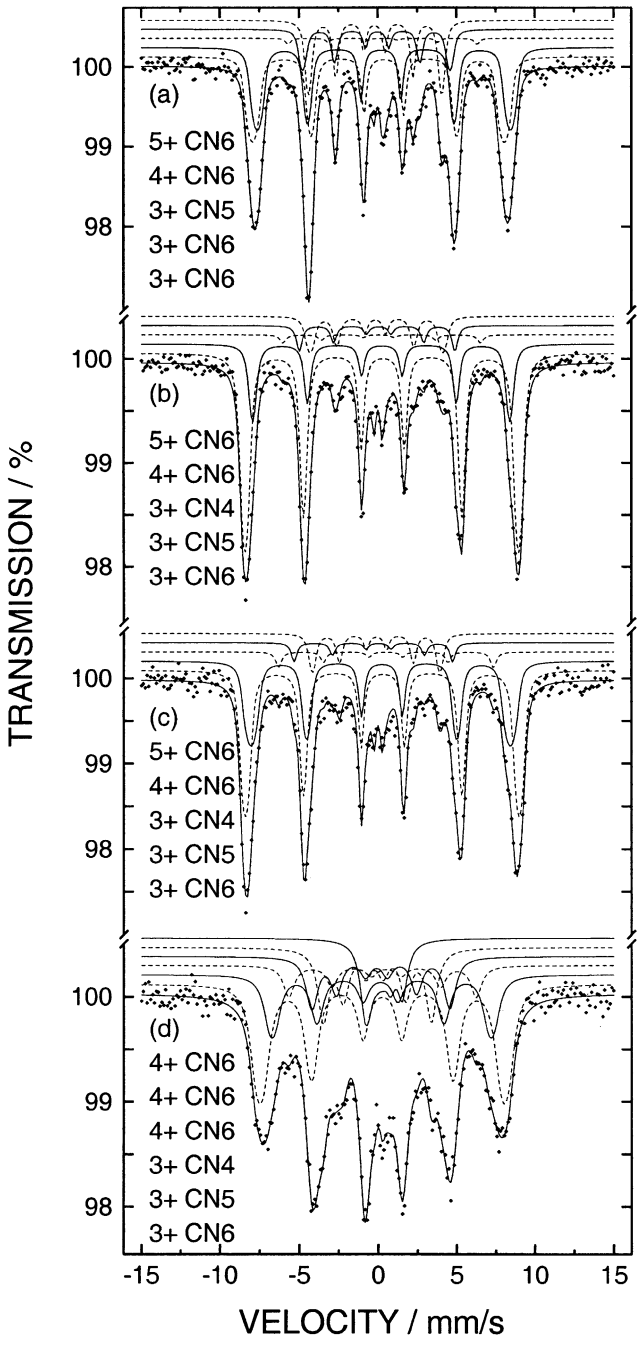

Fig. 4. Selected fitted AF ^{57}Fe Mössbauer spectra (77 K) for (a) $x = 0.50$, $w = 0.017$, (b) $x = 0.50$, $w = 0.144$, (c) $x = 0.67$, $w = 0.249$, and (d) $x = 0.80$, $w = 0.254$. For each spectrum the spectral components are shown above the fitted data in the order presented on the left-hand side.

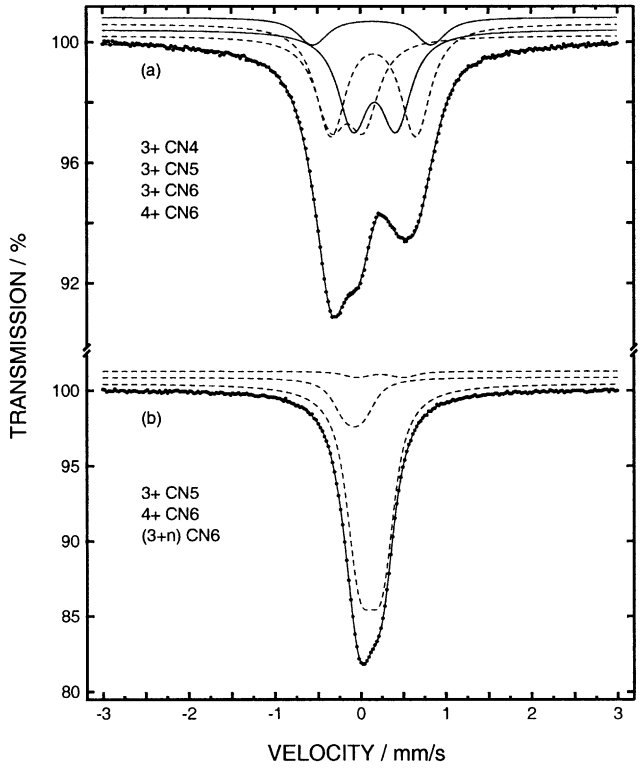

Fig. 5. Selected fitted P ^{57}Fe Mössbauer spectra (296 K) for (a) $x = 0.80$, $w = 0.254$ and (b) $x = 0.45$, $w = 0.016$. For each spectrum the spectral components are shown above the fitted data in the order presented on the left-hand side.

electron transfer dynamics of the disproportionation of Fe^{4+}. Alternatively, the 6 T component may indicate ${}^{CN6}_{AF}Fe^{4+}_{S1}$. Awana et al. [15] suggest a low-spin, P state Fe^{4+} in the temperature region of the charge disproportionation. Presently, indications of an ongoing charge disproportionation were only found for $x = 0.67$, $w = 0.065$ at 77 K. This spectrum shows a high-spin AF state Fe^{4+}, and some Fe^{5+} in addition to marked line broadening.

3.4.4.2. Isomer shifts (AF samples). The isomer shifts for ${}^{CN5}_{AF}Fe^{3+}_{S5/2}$ and ${}^{CN6}_{AF}Fe^{3+}_{S5/2}$ components (Table 2) of around 0.22–0.49 mm/s are well within the expected range for high-spin Fe^{3+}. For ${}^{CN4}_{AF}Fe^{3+}_{S5/2}$ similar values were obtained, except when the component intensity was low and overlap made reliable determination difficult. The high oxidation-state components ${}^{CN6}_{AF}Fe^{4+}_{S2}$ and ${}^{CN6}_{AF}Fe^{5+}_{S3/2}$ have small or negative isomer shift values at 77 K (Table 2). Generally, more negative values were obtained for Fe^{5+}. For $x = 0.50$, $w = 0.144$ and $x = 0.67$, $w = 0.249$ at 296 K the two Fe^{4+} components (21 and 24 T) have a spread in their isomer shift values, the average being close to -0.1 mm/s as expected for ${}^{CN6}_{AF}Fe^{4+}_{S2}$. (The 6 T component has isomer shift 0.05 mm/s, i.e., close to the literature value for Fe^{4+}_{S1} [40].)

3.4.4.3. Isomer shifts (P samples). For oxidized samples at 296 K one of the two CN = 6 components has an isomer shift between that expected for Fe^{3+} and Fe^{4+}. This component, ${}^{CN6}_{P}Fe^{(3+n)+}$, is assigned to a mixed valence state where the formal charge is established from cerimetric titration and lies between 3.2 and 3.4. This

Table 3
Mössbauer parameters (δ, eQV_{zz}, I) for paramagnetic (P) state $Pr_{1-x}Sr_xFeO_{3-w}$ at 296 K

x	w	$^{CN6}_{P}Fe^{3+}$	$^{CN5}_{P}Fe^{3+}$	$^{CN4}_{P}Fe^{3+}$	$^{CN6}_{P}Fe^{(3+n)+}$	$^{CN5}_{P}Fe^{(3+n)+}$	$^{CN6}_{P}Fe^{4+}$
δ (mm/s)							
0.45	0.016(4)		0.3(1)		0.227(6)		0.03(1)
0.50	0.017(5)		0.34(3)[a]		0.209(3)		0.03(3)
0.55	0.033(7)		0.350(6)		0.195(4)		−0.03(2)
0.67	0.065(1)		0.35(2)		0.240(9)		0.008(9)
0.80	0.113(5)		0.197(1)	0.25(1)	0.23(2)		0.008(4)
0.80	0.254(2)	0.281(1)	0.265(3)	0.25 (fixed)			−0.040(4)
1.0	0.158(5)	0.322(3)			0.152(1)		0.027(1)
1.0	0.260(2)	0.376(1)				0.062(4)	−0.127(1)[b]
eQV_{zz} (mm/s)							
0.45	0.016(4)		1.1(6)		0.51(2)		0.40(7)
0.50	0.017(5)		1.4(1)[a]		0.434(8)		0.19(4)
0.55	0.033(7)		0.86(3)		0.49(2)		0.40(7)
0.67	0.065(1)		1.10(fixed)		0.55(2)		0.30(2)
0.80	0.113(5)		1.73(1)	2.61(6)	0.66(1)		0.45(1)
0.80	0.254(2)	1.00(2)	1.98(3)	2.74(7)			0.70(2)
1.0	0.158(5)	2.68(1)			1.261(2)		0.000(5)
1.0	0.260(2)	2.583(2)				0.00(2)	0.757(4)[b]
I (%)							
0.45	0.016(4)		3(1)		82(1)		15(1)
0.50	0.017(5)		3(1)[a]		83(1)		14(1)
0.55	0.033(7)		10(1)		75(1)		15(1)
0.67	0.065(1)		7(2)		50(2)		43(2)
0.80	0.113(5)		26(1)	3(1)	35(1)		36(1)
0.80	0.254(2)	29(1)	35(1)	10(2)			26(1)
1.0	0.158(5)	6.5(2)			47.7(3)		45.9(3)
1.0	0.260(2)	50.2(1)				7.9(1)	41.9(2)[b]

[a] Assignment uncertain, weak component.
[b] Possibly CN5.

mixed-valence species always coexists with a more oxidized Fe^{4+} species. The presence of two mixed components at 296 K may be due to too slow electron transfer between the involved ions. The average valence, $(3+n)+$, shows a certain correlation with the isomer shift value, δ approaching the expected values for high-spin Fe^{3+} when $3+n$ gets closer to 3. Although the second CN = 6 component is assigned to Fe^{4+}, this should not be taken too literally. The 296 K spectra rather indicate a partial merge of Fe^{4+} and Fe^{3+} towards a single $Fe^{(3+n)+}$ valence state that is first attained at more elevated temperature (see Ref. [36]). At 353 K (close to maximum temperature for the present instrument) the spectrum of $Pr_{0.50}Sr_{0.50}FeO_{2.984}$ still shows sign of Fe^{4+} and $Fe^{(3+n)+}$. However, the $Fe^{(3+n)+}$ component has moved to lower δ and has gained intensity at the expense of the Fe^{4+} component.

3.4.4.4. Quadropole splitting. Direct comparison between the quadrupole coupling constants for AF and P samples is not feasible, partly owing to averaging due to statistical variation of the angle θ between the internal magnetic field (B) and the main component of the electric field (V_{zz}) for the P state, and partly owing to a spreading effect of eQV_{zz} due to line broadening and the dynamical charge disproportionation for AF samples. For the P spectra, the rather low eQV_{zz} values for samples in a mixed $Fe^{(3+n)+}$ valence state are indeed signatures of the valence mixing. True mixed-valence states exhibit eQV_{zz} values close to zero, regardless of the local lattice symmetry [37]. In the only P spectrum with pure valence states ($x = 0.80, w = 0.254$) the eQV_{zz} values are substantial, even for the symmetric CN = 6 species. As expected, the CN = 5 and 4 species have generally larger eQV_{zz} values.

3.4.4.5. Component intensities. Assuming a binomial-model distribution of oxygen vacancies the probability for having iron (FeO_{CN}) coordination numbers CN = 6, 5, 4, etc. is given as

$$P(\mathrm{CN}) = \binom{6}{\mathrm{CN}} \left(\frac{3-w}{3}\right)^{\mathrm{CN}} \left[1 - \left(\frac{3-w}{3}\right)\right]^{6-\mathrm{CN}}.$$

The expression neglects defect interactions (cf. lattice-energy calculations on $SrFeO_{3-w}$ [41]), as these cannot be easily included in a purely statistical model. CN < 4 occurs with a probability of less than 2% and is

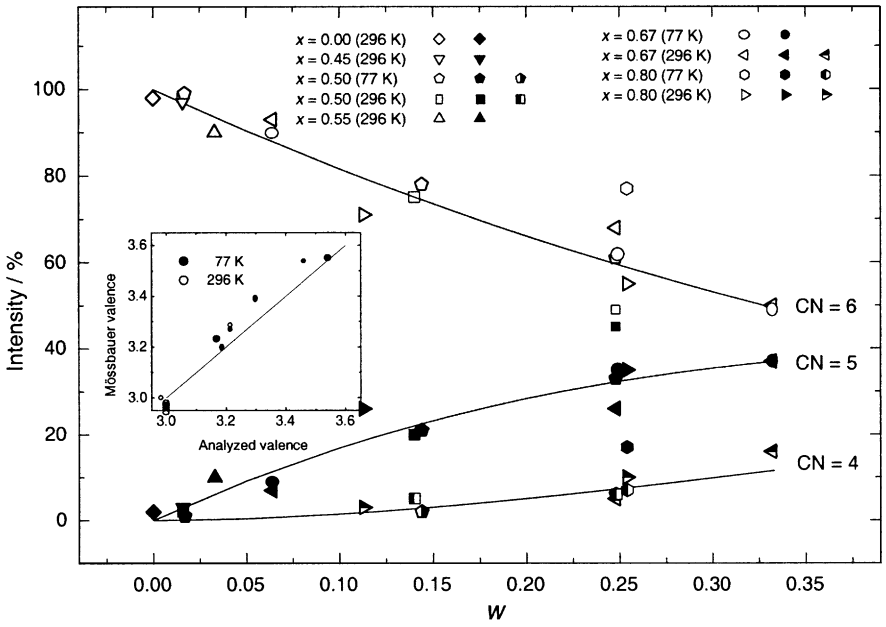

Fig. 6. Experimental Mössbauer intensities ($0 \leqslant x \leqslant 0.80$; 77 and 296 K) vs. w (established by chemical analysis) for all fitted data. Intensities from components assigned to the same coordination numbers are added, regardless of their oxidation and magnetic states. Theoretical curves (lines) according to a binomial-model distribution of O vacancies around Fe are drawn for CN = 6 (open symbols), 5 (filled symbols), and 4 (half-filled symbols). Legends to the symbols are given on the illustration. Inset: Mössbauer valence vs. analyzed valence for AF samples.

neglected in the present treatment. Intensities from components assigned to the same coordination numbers are added, regardless of their valence and magnetic states. These intensities for all fitted data are plotted vs. the analytically determined oxygen content, w, in Fig. 6. The predicted intensity sums according to the binomial model are represented by curves for CN = 6, 5, and 4. For all w and x, the model successfully accounts for the distribution of the oxygen vacancies. The situation deviates from these predictions for $x = 1$ (not shown in Fig. 6; cf. Ref. [36]), where $SrFeO_{3-w}$ exhibits ordered arrangements of oxygen atoms and vacancies. The inset to Fig. 6 shows the good agreement between the average Fe valence derived from the Mössbauer component intensities (AF state) and the corresponding Fe valence obtained by chemical analysis.

3.4.5. *Oxidation-state mixing and disproportionation*

The present findings concur with earlier Mössbauer studies [7,11,13,15,36] in that: (i) Iron may take formal oxidation states $5+$, $4+$, $(3+n)+$, and $3+$ in $Pr_{1-x}Sr_xFeO_{3-w}$ depending on x, w, and T. (ii) Dynamic charge-transfer processes govern the relation between formal oxidation states. (iii) Charge transfer involving $Fe^{(3+n)+}$ takes place at higher temperatures than that of Fe^{5+}. (iv) Different charge-transfer processes may run in parallel, but all charge transfers are completed at a certain temperature.

Starting from an averaged "high"-temperature state the evolution of oxidation states appears to involve five stages: (1) $Fe^{(3+x-2w)+}$, (2) Fe^{4+} in communion with $Fe^{(3+n)+}$, (3) Fe^{4+} in communion with Fe^{3+}, (4) Fe^{5+} in communion with $Fe^{4+}$and Fe^{3+}, and (5) Fe^{5+} in communion with Fe^{3+}. A complicating factor is that the different transitions are continuous and run partly in parallel. Furthermore, the charge-transfer mechanisms are different for the 1-to-2-to-3 and 4-to-5 transitions. It is suggested that the 1-2-3 course involves the conduction band, whereas the 4-to-5 crossing follows the superexchange-like path described by Lindén et al. [38]. The latter can be treated with the mixed-oxidation-state model [38] assuming that electron transfer between neighboring Fe-coordination polyhedra is conveyed via intermediate O atoms. Assuming $w = 0$ and a random distribution of Fe^{3+} and Fe^{5+} in stage (5), the molar fraction of Fe^{4+} in stage (3) is $x_{Fe^{4+}} = 2(x/2)[1-(x/2)]^6$ whereas the molar fraction of Fe^{5+} after completed transition is $x_{Fe^{5+}} = x_{Fe^{4+}}/2 \approx x/2$. The experimental data (Tables 2 and 3) show that although the trends are correct, the predictions are not satisfactory fulfilled (cf. Ref. [38]). The main obstacle for the considerations are the parallel processes involving $Fe^{(3+n)+}$. More generally, discrepancies will appear when oxygen vacancies influence the oxidation-state mixing by reducing (i) the molar fraction of Fe^{5+} (from $x/2$ to $x/2-w$; correspondingly for Fe^{4+}) and (ii) the number of possible charge transfer paths. The latter is hard to assess since correlations will exist between the vacancies and the local configuration of Pr^{3+}, Sr^{2+}, Fe^{3+}, and Fe^{5+}.

3.5. Qualitative comparison of EXAFS data

A number of complexities were encountered in the attempts to extract local structure information from EXAFS Fourier transforms (FT) of $k^3\chi(k)$ data for the Pr L_{III}-, Sr K-, and Fe K-edges. The present account is therefore limited to a qualitative comparison of selected data sets. For the FT data in Fig. 7, the energy ranges and the energy zero offsets were kept constant for each element (10–450, −10.45 eV for Pr; 8–350, −0.6 eV for Sr, and 3–560, 1.93 eV for Fe) to ensure an adequate comparison between different samples. The FTs are corrected for central-atom and oxygen-scattering atom-phase shifts. The peaks located below ~1.5 Å for Fe and ~2.0 Å for Pr and Sr are caused by insufficient background correction. These effects are largest for Pr and Sr, where the atomic background has significant structure due to two-electron excitations.

The effect of introducing Sr on the Pr sublattice is illustrated in Fig. 7a where the first major r(Fe–O) peak at ~2.0 Å in the FT data is seen to appear at slightly lower r values and with appreciably lower intensity for $Pr_{0.50}Sr_{0.50}FeO_{2.983}$ than for $PrFeO_3$. This mirrors the

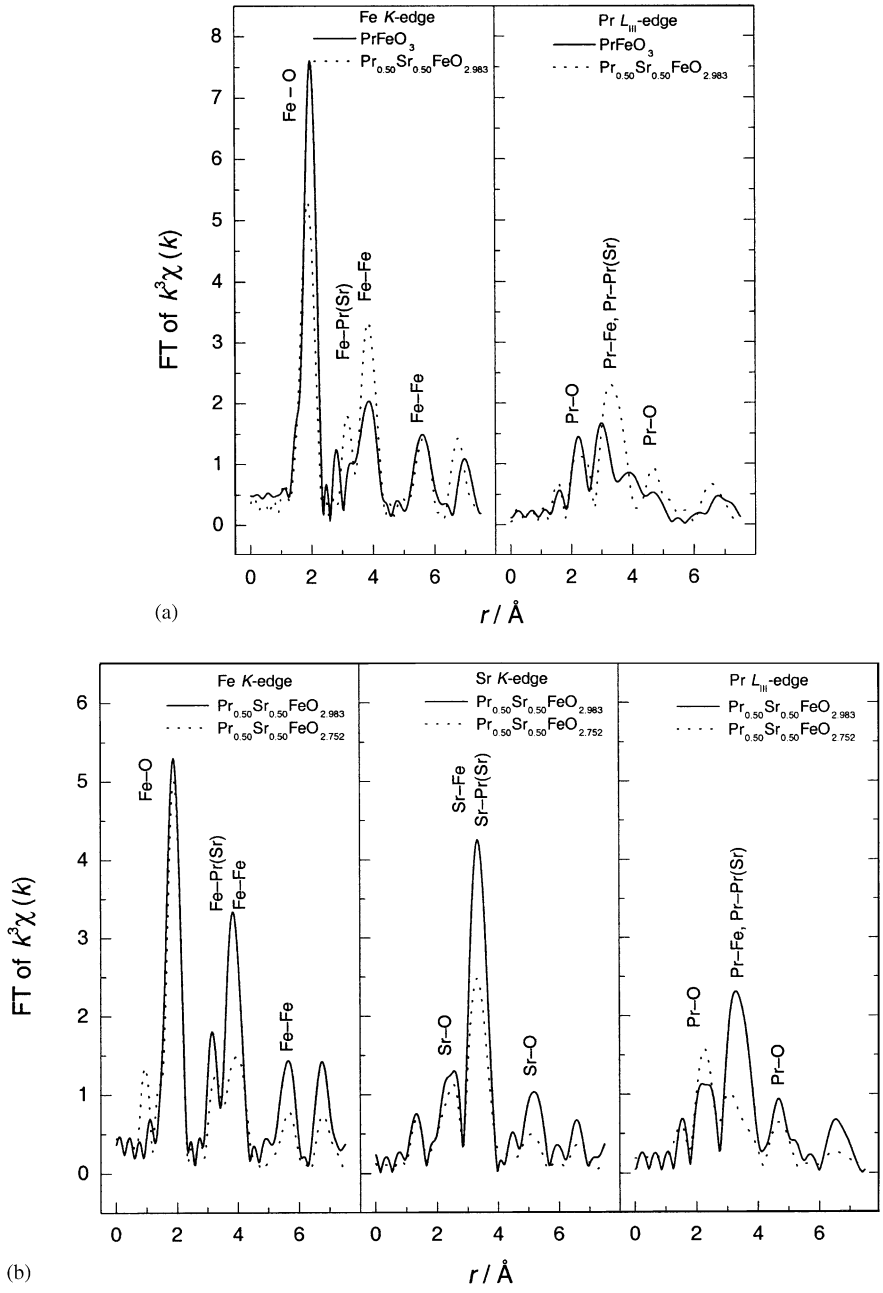

Fig. 7. FT EXAFS (Fe K-, Pr L_{III}-, and Sr K-edge) spectra for (a) $PrFeO_3$ and $Pr_{0.50}Sr_{0.50}FeO_{2.983}$, (b) $Pr_{0.50}Sr_{0.50}FeO_{2.983}$ and $Pr_{0.50}Sr_{0.50}FeO_{2.752}$, (c) $Pr_{0.50}Sr_{0.50}FeO_{2.752}$ and $Pr_{0.33}Sr_{0.67}FeO_{2.668}$, and (d) $Pr_{0.50}Sr_{0.50}FeO_{2.752}$, $Pr_{0.33}Sr_{0.67}FeO_{2.752}$, and $Pr_{0.20}Sr_{0.80}FeO_{2.746}$.

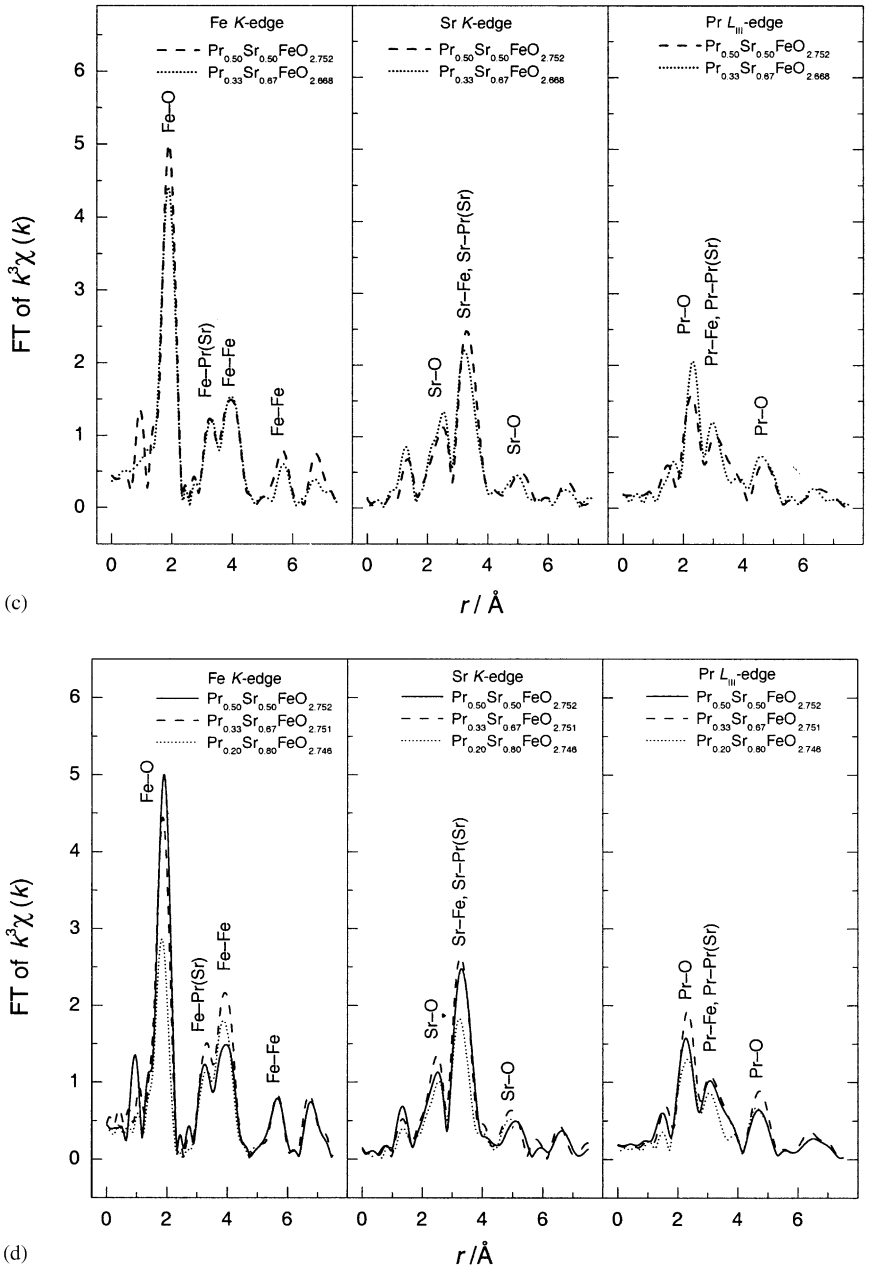

Fig. 7 (*continued*).

increased average oxidation state of Fe and a larger spread in the Fe–O distances owing to increased structural complexity resulting from a mixed *A* site and different Fe-oxidation states. The major peaks at ca. 3 and 3.8 Å become more intense for $Pr_{0.50}Sr_{0.50}$ $FeO_{2.983}$. For the latter peak in particular, this reflects a more collinear Fe–O–Fe arrangement (see Section 3.1) and a larger multiple-scattering contribution. The fourth Fe shell (dominantly Fe–Fe at ~5.5 Å) has a very small multiple-scattering contribution and its intensity is equal for the two samples. This shows that Fe is not shifted off-center of the octahedra as a result of the Sr substitution.

The effect of 50% Sr-for-Pr substitution on the Pr spectrum (Fig. 7a) is to decrease the intensity and broaden the first *r*(Pr–O) peak at ~2.2 Å, to increase the intensity of the second peak (at ~3 Å for $PrFeO_3$) which merges with the third peak and becomes significantly shifted to higher *r* values (mirroring Pr–Sr/Pr and Pr–Fe environments), and to make the fourth peak at ~4.8 Å more pronounced. These changes reflect two basic aspects; increased overall structural symmetry consequent on reduced octahedral tilting and increased disorder at the Pr/Sr and O sites.

For the Fe spectrum (Fig. 7b) the introduction of oxygen vacancies in $Pr_{0.50}Sr_{0.50}FeO_{2.983}$ reduces the

intensity beyond the first peak. This reflects increased local disorder which must also involve the Fe sublattice owing to the intensity reduction of the ~5.5 Å single-scattering peak. The average structure of $Pr_{0.50}Sr_{0.50}FeO_{2.752}$ is cubic. Low peak intensities become evident when inspecting the fit to all EXAFS edges according to the $Pm\bar{3}m$ model and this indicates large structural disorder. A qualitative, combined EXAFS and PND study will be presented later.

The effects of introducing additional oxygen vacancies from $w = 0.25$ to 0.33 (Fig. 7c), and increasing the Sr-substitution level from $x = 0.50$ to 0.80 ($w = 0.25$; Fig. 7d) are rather minor both with regard to intensities and distances. In accordance with expectations, r(Fe–O) decreases in the sequence $x = 0.50$, 0.67–0.80 for $w \approx 0.25$ (increased amount of higher-valent Fe species).

3.6. Concluding remarks

The present study has shown that:

(i) The oxygen saturated $Pr_{1-x}Sr_xFeO_{3-w}$ ($w \approx 0.00$) gradually changes symmetry from *Pnma* to *Imma* as a function of substitution (x), a hitherto unknown situation for ferrites. At high substitution levels the symmetry converts (after a two-phase region) to $R\bar{3}c$.

(ii) The average structure of the most reduced $Pr_{1-x}Sr_xFeO_{3-w}$ samples ($w \approx 0.109$–0.332) is reasonably well described by $Pm\bar{3}m$ symmetry. However, the local structure appears to deviate significantly, the distinctions remaining unidentified. The introduction of oxygen vacancies affects the local order for all cation sites. A simple binomial expression describes the distribution of different Fe–O coordination polyhedra.

(iii) The Néel temperature for G-type antiferromagnetic order depends strongly on the average oxidation state for iron.

(iv) Depending on x, w, and temperature the formal species Fe^{5+}, Fe^{4+}, $Fe^{(3+n)+}$ (n variable), and Fe^{3+} occur. At low temperature Fe^{5+} rules together with Fe^{3+} whereas at sufficiently high temperature a global average Fe-valence state probably rules. The iron-valence states undergo temperature-dependent fluctuations that originate from electron transfer via oxygen atoms or via the conduction band.

Acknowledgments

MS is grateful to the Research Council of Norway for financial support. The assistance of Lorrie Murphy at BL 8.1 and Fred Mosselmans at BL 9.2, SRS, Daresbury, are gratefully acknowledged. T. Pietari and M. Matvejeff are acknowledged for performing Mössbauer measurements.

References

[1] M. Takano, N. Nakanishi, Y. Takeda, S. Naka, T. Takeda, Mater. Res. Bull. 12 (1977) 923.
[2] P.M. Woodward, D.E. Cox, E. Moshopoulou, A.W. Sleight, S. Morimoto, Phys. Rev. B 62 (2000) 844.
[3] M. Takano, N. Nakanishi, Y. Takeda, S. Naka, J. Phys. Colloq. 40 (1979) C2–313.
[4] Y. Takano, S. Naka, M. Takano, J. Phys. Colloq. 40 (1979) C2–331.
[5] M. Takano, J. Kawachi, N. Nakanishi, Y. Takeda, J. Solid State Chem. 39 (1981) 75.
[6] P.D. Battle, T.C. Gibb, S. Nixon, J. Solid State Chem. 77 (1988) 124.
[7] P.D. Battle, T.C. Gibb, S. Nixon, J. Solid State Chem. 79 (1989) 86.
[8] S.E. Dann, D.B. Currie, M.T. Weller, M.F. Thomas, A.D. Al-Rawwas, J. Solid State Chem. 109 (1994) 134.
[9] E. Garcia-Gonzalez, M. Parras, J.M. Gonzalez-Calbet, M. Vallet-Regi, J. Solid State Chem. 124 (1996) 278.
[10] T. Ishikawa, S.K. Park, T. Katsufuji, T. Arima, Y. Tokura, Phys. Rev. B 58 (1998) R13326.
[11] I. Nowik, I. Felner, V.P.S. Awana, J. Magn. Magn. Mater. 192 (1999) 67.
[12] S.K. Park, T. Ishikawa, Y. Tokura, J.Q. Li, Y. Matsui, Phys. Rev. B 60 (1999) 10788.
[13] Y.R. Uhm, S.W. Lee, K.-T. Park, Y. Tomioka, Y. Tokura, C.S. Kim, J. Appl. Phys. 87 (2000) 4873.
[14] H.W. Brinks, H. Fjellvåg, A. Kjekshus, B.C. Hauback, J. Solid State Chem. 150 (2000) 233.
[15] V.P.S. Awana, S.X. Dou, I. Felner, I. Novik, S.K. Malik, A. Mehta, R. Singh, A.V. Narlikar, W.B. Yelon, J. Appl. Phys. 83 (1998) 7312.
[16] V.P.S. Awana, J. Nakamura, J. Lindén, M. Karppinen, H. Yamauchi, Solid State Commun. 119 (2001) 159.
[17] P.D. Battle, T.C. Gibb, P. Lightfoot, J. Solid State Chem. 84 (1990) 237.
[18] Y. Takeda, K. Kanno, T. Takeda, Y. Yamamoto, M. Takano, N. Nakayama, Y. Bando, J. Solid State Chem. 63 (1986) 237.
[19] Bengt Noläng, Program UNITCELL, Version 0.9, Institute of Chemistry, Uppsala University, Uppsala, Sweden, 1997.
[20] A.C. Larson, R.B. Von Dreele, Program GSAS, General Structure Analysis System, LANSCE, MS-H 805, Los Alamos National Laboratory, Los Alamos, NM 87545, USA, 1998.
[21] N. Binsted, PAXAS, Program for the Analysis of X-ray Absorption Spectra, University of Southampton, UK, 1988.
[22] N. Binsted, M.J. Pack, M.T. Weller, J. Evans, J. Am. Chem. Soc. 118 (1996) 10200.
[23] M. Marezio, J.P. Remeika, P.D. Dernier, Acta Crystallogr. Sect. B 26 (1970) 2008.
[24] A.M. Glazer, Acta Crystallogr. Sect. B 28 (1972) 3385.
[25] P.M. Woodward, Acta Crystallogr. Sect. B 53 (1997) 32.
[26] P.M. Woodward, T. Vogt, D.E. Cox, A. Arulraj, C.N.R. Rao, P. Karen, A.K. Cheetham, Chem. Mater. 10 (1998) 3652.
[27] P.M. Woodward, J. Appl. Crystallogr. 30 (1997) 206.
[28] R.D. Shannon, Acta Crystallogr. Sect. A 32 (1976) 751.
[29] J.P. Hodges, S. Short, J.D. Jorgensen, X. Xiong, B. Dabrowski, S.M. Mini, C.W. Kimball, J. Solid State Chem. 151 (2000) 190.
[30] D. Trevis, J. Appl. Phys. 36 (1965) 1033.
[31] P.D. Battle, T.C. Gibb, S. Nixon, J. Solid State Chem. 79 (1989) 75.

[32] G. Thornton, B.C. Toefield, A.H. Hewat, J. Solid State Chem. 61 (1986) 301.
[33] J.B. MacChesney, R.C. Sherwood, J.F. Potter, J. Chem. Phys. 43 (1965) 1907.
[34] J.S. Smart, Effective Field Theories of Magnetism, Saunders, Philadelphia, 1966.
[35] A. Wattiaux, J.C. Grenier, M. Pouchard, P. Hagenmuller, J. Electrochem. Soc. 134 (1987) 1718.
[36] L. Fournés, Y. Potin, J.C. Grenier, G. Demazeau, M. Pouchard, Solid State Commun. 62 (1987) 239.
[37] J. Lindén, M. Lippmaa, P. Karen, A. Kjekshus, M. Karppinen, J. Solid State Chem. 138 (1998) 87.
[38] J. Lindén, P. Karen, A. Kjekshus, J. Miettinen, T. Pietari, M. Karppinen, Phys. Rev. B 60 (1999) 15 251.
[39] K. Kuzushita, S. Morimoto, S. Nasu, S. Nakamura, J. Phys. Soc. Jpn. 69 (2000) 2767.
[40] N.N. Greenwood, T.C. Gibb, Mössbauer Spectroscopy, Chapman & Hall, London, 1971.
[41] S. Stølen, Personal communication.